ORIGINAL ARTICLE

Molecular engineering of antibodies for site-specific conjugation to lipid polydopamine hybrid nanoparticles

Hobin Yang[a,†], Quoc-Viet Le[b,†], Gayong Shim[b,*], Yu-Kyoung Oh[b,*], Young Kee Shin[a,c,d,*]

[a]Laboratory of Molecular Pathology and Cancer Genomics, College of Pharmacy and Research Institute of Pharmaceutical Sciences, Seoul National University, Seoul 08826, Republic of Korea
[b]College of Pharmacy and Research Institute of Pharmaceutical Sciences, Seoul National University, Seoul 08826, Republic of Korea
[c]Molecular Medicine and Biopharmaceutical Sciences, Graduate School of Convergence Science and Technology, Seoul National University, Seoul 08826, Republic of Korea
[d]Bio-MAX, Seoul National University, Seoul 08826, Republic of Korea

Abstract Conjugation of antibodies to nanoparticles allows specific cancer targeting, but conventional conjugation methods generate heterogeneous conjugations that cannot guarantee the optimal orientation and functionality of the conjugated antibody. Here, a molecular engineering technique was used for site-specific conjugation of antibodies to nanoparticles. We designed an anti-claudin 3 (CLDN3) antibody containing a single cysteine residue, h4G3cys, then linked it to the maleimide group of lipid polydopamine hybrid nanoparticles (LPNs). Because of their negatively charged lipid coating, LPNs showed high colloidal stability and provided a functional surface for site-specific conjugation of h4G3cys. The activity of h4G3cys was tested by measuring the binding of h4G3cys-conjugated LPNs (C-LPNs) to CLDN3-positive tumor cells and assessing its subsequent photothermal effects. C-LPNs specifically recognized CLDN3-overexpressing T47D breast cancer cells but not CLDN3-negative Hs578T breast cancer cells. High binding of C-LPNs to CLDN3-overexpressing T47D cells resulted in significantly higher temperature generation upon NIR irradiation and potent anticancer photothermal efficacy. Consistent with this,

intravenous injection of C-LPNsin a T47D xenograft mouse model followed by NIR irradiation caused remarkable tumor ablation compared with other treatments through high temperature increases. Our results establish an accurate antibody-linking method and demonstrate the possibility of developing therapeutics using antibody-guided nanoparticles.

1. Introduction

Antibodies have been used for controlling the distribution of functional nanoparticles to target tissues[1−5]. Trastuzumab, a human epidermal growth factor receptor 2 (HER2)-targeting antibody, has been used to enhance the delivery of liposomes to breast cancer cells[2,5]. An anti-CD44v6 antibody was shown to improve the photothermal efficacy of gold nanoparticles toward gastric cancer stem cells compared with a non-modified carrier[1]. In another study, a single chain variable fragment (scFv) of HER-2 was used to enhance the imaging of silica nanoparticles accumulated in tumor tissues[3]. Recently, an antibody against PD-L1 (programmed death-ligand 1) was used to direct the binding of nanoparticles to PD-L1-expressing tumor cells[6].

A common feature of these studies is that the antibodies used were covalently tethered on the nanoparticle surface, typically accomplished using a coupling method[7,8]. Despite forming a stable covalent amide bond[9], carbodiimide coupling chemistry is non-specific, generating heterogeneous conjugation of antibodies on the surface of nanoparticles. Such nonspecific modifications make it difficult to control the orientation of conjugated antibodies on nanoparticles and can reduce the target specificity of the antibody[10].

A number of chemical linker approaches have been investigated for achieving site-specific conjugation of antibodies onto nanoparticles. For example, an alkyne−nitrone cycloaddition method has been used to conjugate scFv antibody to super paramagnetic nanoparticles[11], antibody light chains have been coupled to gold nanoparticles using an indole-derived linker[12]; and heterobifunctional linkers have been used to conjugate anti-ephrin type-A receptor 2 Fab moieties to polymeric micelles[13]. Although these methods have made progress in site-specific conjugation of antibodies to nanoparticles, the multiple, complicated synthesis steps required to achieve specificity remain a challenge.

In this study, as an alternative to a complex chemical linker strategy, we used molecular engineering of the antibody for simple, site-specific conjugation to nanoparticles. As a model antibody, we chose the antibody h4G3, which targets claudin 3 (CLDN3), a cancer biomarker that is overexpressed in various cancers[14,15], and engineered the antibody by genetically modifying it to introduce a cysteine group in its light chain constant region, yielding the modified antibody, h4G3cys. Genetic introduction of a cysteine group in the antibody enabled site-specific conjugation onto maleimide groups of lipid and polydopamine (PDA) hybrid nanoparticles. Here, we report that the site-specific conjugation of h4G3cys to nanoparticles improves binding to CLDN3-positive tumor cells, and provides the photo-responsive tumor-ablation effect.

2. Materials and methods

2.1. Expression and purification of a cysteine-engineered anti-CLDN3 human monoclonal antibody

For site-specific antibody conjugation, residue Q124 in the light chain of h4G3 was replaced with cysteine[16]. Stable h4G3cys-expressing CHO-S cells were subsequently established by cloning the light chain containing the cysteine mutation (Q124C) and heavy chain of h4G3 into a Freedom pCHO 1.0 vector (Thermo Fisher Scientific, Inc., Waltham, MA, USA) and transfecting it into Freedom CHO-S cells (Thermo Fisher Scientific, Inc.) in accordance with the manufacturer's instructions. The resulting h4G3cys-transfected CHO-S cells were incubated at 37 °C in an orbital shaker (130 rpm) with a humidified atmosphere of 8% CO_2 for 2 weeks, with feeding of 4 g/L glucose on Days 3 and 5, and 6 g/L glucose on Day 7. The culture supernatant was then loaded onto MabSelect SuRe Protein A resin (GE Healthcare, Piscataway, NJ, USA) and washed with five column volumes of 35 mmol/L sodium phosphate and 500 mmol/L NaCl (pH 7.2), after which bound antibody was eluted with five column volumes of 0.1 mol/L sodium citrate (pH 3.6) and neutralized using 1 mol/L Tris-HCl (pH 8.0). Buffer exchange and concentration were accomplished using an Amicon Ultra-15 centrifugal concentrator (Merck Millipore, Billerica, MA, USA). The antibody was quantified using a Cedex Bio Analyzer (Roche, Indianapolis, IN, USA), and the molecular weight of the antibody was confirmed by sodium dodecyl sulfate-polyacrylamide gel electrophoresis (SDS-PAGE) under reducing and non-reducing conditions.

2.2. Thiol reactivity analysis and site-specific biotinylation of h4G3cys

The reactivity of thiol groups was assessed by measuring the formation of 4-mercaptopyridine using UV−Vis spectrometry. A 7-μmol/L solution of purified h4G3cys was reacted with a 500 μmol/L solution of 4,4′-dithiopyridine (4-PDS) in 0.1 mol/L sodium phosphate buffer (pH 6.0). After allowing the reaction to proceed for 15 min at room temperature, absorbance was measured at 324 nm using a UV−Vis spectrometer (Ultrospec 2100 Pro; Amersham Biosciences, Uppsala, Sweden). A standard curve was obtained by titration of N-acetyl-L-cysteine with 4-PDS. h4G3cys was biotinylated using an EZ-Link Maleimide-PEG Solid Phase Biotinylation Kit (Thermo Fisher Scientific) in accordance with the manufacturer's instructions. Biotin conjugation was confirmed by Western blotting using streptavidin-horse radish peroxidase (SHRP, Sigma−Aldrich, St. Louis, MO, USA).

2.3. Synthesis of polydopamine core nanoparticles

Polydopamine (PDA) was synthesized by polymerizing dopamine under alkaline conditions, as described previously[6]. Briefly, 50 mg dopamine hydrochloride (Sigma−Aldrich) was dissolved in 25 mL triple distilled water (TDW), and the resulting dopamine solution was slowly mixed with 1 mol/L sodium hydroxide solution until a pH of 9.6 was reached. The polymerization reaction was maintained at room temperature for 18 h with vigorous magnetic stirring, and then was centrifuged (Merck Millipore) at 13,000×g for 20 min. The pellet was washed with TDW by repeating three cycles of centrifugation, and the resulting PDA core nanoparticles (PNs) were dispersed in TDW and stored at 4 °C until use.

2.4. Preparation of antibody-conjugated lipid-polydopamine hybrid nanoparticles

For site-specific conjugation of antibody onto nanoparticles, PNs were first shelled with a layer of maleimide-functionalized lipid using a co-extrusion technique[17]. All lipids—1,2-dipalmitoyl-sn-glycero-3-phosphocholine (DPPC), 1,2-dipalmitoyl-sn-glycero-3-phosphorylglycerol (DPPG), 1,2-distearoyl-sn-glycero-3-phosphoethanolamine-N-[maleimide(polyethylene glycol)-2000] (ammonium salt, DSPE-malPEG$_{2000}$), fluorescein isothiocyanate-conjugated PEG lipid (DSPE-PEG$_{2000}$-FITC), cyanine 5-conjugated PEG lipid (DSPE-PEG$_{2000}$-Cy5)—were purchased from Avanti Polar Lipids (Birmingham, AL, USA). DPPC, DPPG and DSPE-malPEG$_{2000}$ were dissolved in co-solvent (chloroform:methanol, 4:1, v/v) at a molar ratio of 7:3:0.1. In some experiments, DSPE-PEG$_{2000}$-FITC was added to the lipid mixture at 0.02% (mol/mol) of total lipids to allow nanoparticle tracking. For in vivo distribution study, DSPE-PEG$_{2000}$-Cy5 was added to the lipid mixture at 0.1% (mol/mol) of total lipids. The lipid solution was evaporated under vacuum to generate a thin lipid film, which was subsequently rehydrated with 1 mL of a 10 mg/mL PN solution. The resulting solution was extruded through a 0.4 μm polycarbonate membrane (Merck Millipore), yielding hybrid lipid polydopamine nanoparticles (LPNs). For antibody conjugation with LPNs, 100 μL of isotype IgG (Q124C) or h4G3cys (10 mg/mL) was mixed with 1 mL of LPNs, and the reaction was left overnight at 4 °C. For the same thiol-maleimide conjugation reaction between antibody and LPNs, we used the isotype IgG, Q124C, which is also genetically engineered to express cysteine at Q124 residue. After the reaction, free antibody was removed by centrifugation at 13,000×g for 10 min (Merck Millipore). The pellet was rehydrated with 1 mL 5% glucose and extruded using a 0.4 μm polycarbonate membrane. The resulting isotype IgG antibody-modified LPNs (IG-LPNs) and anti-CLDN3 antibody h4G3cys-modified LPNs (C-LPNs) were collected and stored at 4 °C.

2.5. Characterization of h4G3-lipid-coated PDA nanoparticles (C-LPNs)

C-LPNs were characterized with respect to morphology, elemental mapping, size, zeta potential, lipid coating, and antibody conjugation efficiency. The morphology of C-LPNs was visualized by transmission electron microscopy (TEM) using a JEM1010 system (JEOL, Tokyo, Japan). Prior to visualization, C-LPNs were briefly stained with a 1% uranyl acetate solution. Elemental mapping of carbon, oxygen, nitrogen and phosphorus present in

C-LPNs was performed using energy dispersive X-ray spectroscopy-scanning transmission electron microscopy (EDS-STEM) using a JEM-2100F system (JEOL). Hydrodynamic size, size distribution, and zeta potentials were measured using dynamic light scattering and laser Doppler microelectrophoresis at an angle of 22° using an ELS8000 instrument (Photal, Osaka, Japan). The lipid content of nanoparticles was quantified by measuring phosphorus content using a phosphate assay[18]. The content of immobilized antibody on nanoparticles was measured using a Cedex Bio Analyzer (Roche). The photothermal ability of LPNs was investigated by irradiating with a 808 nm laser using a diode laser beam (BWT Beijing Ltd., Beijing, China) at an output power of 1.5 W. Real-time temperatures were measured using an infrared camera (FLIR E60; FLIR Systems Inc., Danderyd, Sweden).

2.6. Measurement of photothermal conversion efficiency

To measure the photothermal efficiency, 500 μL of samples (0.4 mg/mL) in a Quartz cuvette was irradiated with NIR laser (808 nm) at a power 1.5 W using a diode laser beam (BWT Beijing Ltd., Beijing, China). When the temperatures of the samples reached maximum steady-state, the laser was turned off. The change of temperatures during laser irradiation period was recorded. Photothermal conversion efficiency (η) of samples was calculated from the following Eqs. (1)−(4) [19]:

$$\eta = \frac{hs(T_{\text{Max}} - T_{\text{Surr}}) - Q_{\text{Dis}}}{I(1 - 10^{-A_{808}})} \quad (1)$$

$$hs = \frac{m_D C_D}{\tau_s} \quad (2)$$

$$t = -\tau_s \text{Ln}(\theta) \quad (3)$$

$$\theta = \frac{T - T_{\text{sur}}}{T_{\text{Max}} - T_{\text{Surr}}} \quad (4)$$

where h is the heat transfer coefficient, s is the surface area of the container. The values of hs were obtained from Eqs. (2)−(4). In Eq. (2), τ_s is the time constant measured from the slope of linear regression line plotted by time t and $-\ln(\theta)$. T_{max} is the maximum steady-state temperature, and T_{surr} is the surround temperature. Q_{Dis} is the heat associated with the light absorbance of control sample (water). I is the input power, and A_{808} is the absorbance of sample at 808 nm.

2.7. Cell lines

The human breast cancer cell lines, Hs578T, T47D, MCF-7, and ovarian cancer cell lines, OVCAR-3 and Caov-3, were purchased from the Korean Cell Line Bank (KCLB; Seoul, Republic of Korea). The human ovarian cancer cell line TOV-112D was from American Type Culture Collection (ATCC; Manassas, VA, USA). TOV-112D cells were transfected for stable expression of CLDN3 as described in previous study[43]. TOV-112D cells was cultured in 1:1 mixture of Media199/MCDB medium (HyClone, Logan, UT, USA) containing 15% FBS, 100 unit/mL penicillin, and 100 μg/mL streptomycin. T47D, MCF-7, OVCAR-3 cells were cultured in RPMI-1640 medium (HyClone) supplemented with 10% fetal bovine serum (FBS; HyClone), 100 U/mL penicillin, and 100 μg/mL streptomycin. Caov-3 and Hs578T cells were cultured

in Dulbecco's modified Eagle's medium (DMEM, HyClone) supplemented with 10% FBS (HyClone), 100 U/mL penicillin, and 100 µg/mL streptomycin. The cells were incubated at 37 °C in a humidified 5% CO_2 atmosphere.

2.8. Cell-based binding kinetics

The binding kinetics of h4G3cys against CLDN3 on the cell membrane were determined using LigandTracer Green (Ridgeview Instruments AB, Vänge, Sweden). The CLDN3-negative TOV-112D cells were used as reference cells, and CLDN3-expressing CLDN3/TOV-112D cells were for target cells. The cells were seeded on 100 mm culture dish at a density of 3×10^5 cells/mL. Next day, the cells were placed in the LigandTracer Green device. After baseline equilibrium, DyLight dye 488-labeled h4G3cys was sequentially added to the cells with 3 and 9 nmol/L. Data were analyzed by TraceDrawer (Ridgeview Instruments AB). For antibody affinity test, 2.5×10^5 cells were incubated for 1 h with 2.5 µg/mL of h4G3 or h4G3cys. Cells were stained with FITC-conjugated goat anti-human IgG (Jackson Immunoresearch Laboratories, West Grove, PA, USA) at 1:100 ratio. Stained cells were analyzed using a BD FACSCalibur system equipped with Cell Quest Pro software (BD Biosciences).

2.9. Cellular uptake assay

Cellular uptake of C-LPNs was evaluated using flow cytometry, immunofluorescence, and TEM imaging. For flow cytometry, Hs578T and T47D cells were seeded on a 24-well plate at a density of 2×10^5 cells/well. After 48 h, cells were treated with 50 µg/mL of FITC-labeled IG-LPNs or C-LPNs for 1 h at 37 °C. The cells were then detached using an enzyme-free, phosphate-buffered saline (PBS)-based cell dissociation buffer (Thermo Fisher Scientific, Inc.) and incubated for 1 h with Alexa Flour 647-conjugated goat anti-human IgG (Biolegend Inc., San Diego, CA, USA), diluted 1:500. Stained cells were washed three times and analyzed using a BD FACSCalibur system equipped with Cell Quest Pro software (BD Biosciences, San Jose, CA, USA).

For immunofluorescence, Hs578T and T47D cells were seeded on a 4-well slide, grown to 80% confluence, and treated with 100 µg/mL of FITC-labeled IG-LPNs or C-LPNs for 1 h at 37 °C. Cells were then fixed by incubating with 4% formaldehyde for 15 min and then were incubated with Alexa 555-conjugated anti-human IgG antibody (Thermo Fisher Scientific, 1:500) for 1 h. Cells were counterstained with the nuclear dye, Hoechst 33342 (Invitrogen, Carlsbad, CA, USA), and coverslip-mounted using Fluoromount Aqueous Mounting Medium (Sigma−Aldrich). Images were observed using an LSM 700 ZEISS laser-scanning confocal microscope (Carl Zeiss, Jena, Germany), and the data were processed using ZEN confocal software (Carl Zeiss).

For cellular TEM images, Hs578T and T47D cells were cultured to ∼80% confluence in 100 mm cell culture dishes and then treated with 300 µg/mL of C-LPNs for 1 h at 37 °C. Cells were washed with PBS and harvested, and the resulting cell pellets were fixed with Karnovsky's solution overnight at 4 °C. After washing with 0.05 mol/L sodium cacodylate buffer, cell pellets were fixed with 1% osmium tetroxide and stained with 0.5% uranyl acetate. Pellets were then dehydrated using a gradual series of ethanol and immersed in propylene oxide, which was gradually replaced with Spurr's resin. The cell pellets were then cut into thin sections and observed by TEM (TalosL120C; Thermo Fisher Scientific, Inc.).

2.10. In vitro photothermal anticancer efficacy

The Hs578T and T47D cells were seeded on a 24-well plate at a density of 2×10^5 cells/well. After a 48 h incubation, cells were treated with 300 µg/mL of IG-LPNs or C-LPNs for 1 h at 37 °C. Thereafter, cells were detached with enzyme-free, PBS-based cell dissociation buffer (Thermo Fisher Scientific, Inc.) and centrifuged at 3000 rpm for 5 min (Merck Millipore). The cell pellets were irradiated for 5 min with an NIR laser (808 nm) at 1.5 W power using a diode laser beam (BWT Beijing Ltd.). Temperature was measured using an infrared camera (FLIR E60). The irradiated cells were seeded on a 96-well plate and incubated for 24 h at 37 °C. The viability of cells was measured using a water soluble tetrazolium salt (WST) assay and visualized by staining live cells and dead cells using calcein-AM (Biolegend Inc.) and propidium iodide (Biomax, Gongneung-dong, Seoul, Republic of Korea), respectively.

2.11. In vivo distribution in a nude mouse xenograft model

Animal studies were conducted according to Guidelines for the Care and Use of Laboratory Animals of the Institute of Laboratory Animal Resources in Seoul National University (approved animal experimental protocol number, SNU-190216-1). A mouse xenograft model was prepared by subcutaneously injecting T47D cells $(1 \times 10^7$ cells in 100 µL PBS) into athymic nude mice (Orient Bio Inc., Seongnam, Republic of Korea) implanted with 17β-estradiol pellets (Innovative Research of America, Sarasota, FL, USA). After tumor volumes reached 300 mm^3, tumor-bearing mice were intravenously administered with 2 mg of Cy5-labelled IG-LPNs or Cy5-labelled C-LPNs per mouse. For the fluorescence labelling, Cy5-conjugated lipid was used. Whole body distribution of the Cy5-labelled nanoparticles was imaged by near infrared fluorescent imaging system AMI-HT (Spectral Imaging Instruments, Tucson, AZ, USA) at various time points. At 48 h post-injection, main organs and tumor tissues were collected for *ex vivo* imaging.

2.12. In vivo photothermal anticancer efficacy in a nude mouse xenograft model

A mouse xenograft model was prepared by subcutaneously injecting T47D cells $(1 \times 10^7$ cells in 100 µL PBS) into athymic nude mice (Orient Bio Inc.) implanted with 17β-estradiol pellets (Innovative Research of America). After tumor volumes reached ∼300 mm^3, tumor-bearing mice were intravenously administered 2 mg of IG-LPNs or C-LPNs per mouse. Twenty-four hours later, mice were irradiated at three sites on the tumor with NIR (808 nm) for 5 min at a power of 1.2 W using a light-emitting diode (BWT Beijing), and then the temperature of mice was measured using an infrared camera (FLIR Systems Inc.). Tumor volume and body weight were measured twice a week. Tumor volume was calculated according to Eq. (5):

$$\text{Tumor volume} = \text{Length} \times \text{Width}^2/2 \tag{5}$$

2.13. Histological staining and in vivo cell apoptosis assay

A mouse xenograft model was prepared by subcutaneously injecting T47D cells $(1 \times 10^7$ cells in 100 µL PBS) into athymic nude mice (Orient Bio Inc.) implanted with 17β-estradiol pellets (Innovative Research of America). After tumor volumes reached 300 mm^3, T47D tumor-bearing mice were intravenously

administered with 2 mg of IG-LPNs or C-LPNs per mouse. One day post-dose, mice were irradiated with NIR. Next day, tumors were extracted, fixed in 4% paraformaldehyde for 24 h, and embedded in paraffin. Tumor tissues were sectioned at a thickness of 3 µmol/L and stained with hematoxylin and eosin (H&E). Apoptotic cells *in vivo* were detected by terminal deoxy nucleo-tidyl transferase-mediated dUTP Nick end labeling (TUNEL) assay using ApopTag® Peroxidase *In Situ* Apoptosis Detection Kit (Merck Millipore) according to the manufacturer's protocols. The tumor tissues were observed using a Pannoramic MIDI digital slide scanner (3DHISTECH Ltd., Budapest, Hungary).

2.14.   Statistical analysis

Two-way analysis of variance (ANOVA) was used for assessing the significance of differences between groups. Data were analyzed using GraphPad Prism 7 (GraphPad Software), and a P-value <0.05 was considered statistically significant.

3.   Results

3.1.   Preparation and physical characterization of C-LPNs

C-LPNs were prepared by site-specific conjugation of the cysteine-engineered antibody, h4G3cys, to maleimide groups of LPNs. h4G3cys was produced by mutating Q124 in the light chain of h4G3 to cysteine, as previously described[15]. The expression pattern (Supporting Information Fig. S1) and binding affinity (Supporting Information Fig. S2) of h4G3cys were similar to those of h4G3, but h4G3cys showed two free thiol groups per an antibody and 9.5-fold higher thiol reactivity ratio compared with h4G3 (Fig. 2A). Site-specific conjugation to the free thiol groups in h4G3cys was evaluated using maleimide-PEG$_2$-biotin, and specific conjugation of maleimide-PEG$_2$-biotin to the light chain of h4G3cys compared with the light chain of h4G3 was confirmed by Western blotting using streptavidin-horse radish peroxidase (SHRP, Fig. 2B). The binding affinity of h4G3cys to CLDN3/TOV-112D cells was 5.24 nmol/L in the 'one-to-one two-state' model (Fig. 2C). In the 'one-to-two' model (Fig. 2D), the first binding affinity (K_{D1}) was 11.00 nmol/L and the second binding affinity (K_{D2}) was 0.58 nmol/L (Supporting Information Table S1). Flow cytometry analysis revealed that h4G3cys and h4G3 did not show notable differences in binding patterns to various cell lines such as CLDN3-negative (TOV-112D, Hs578T), CLDN3-stable expressing (CLDN3/TOV-112D), and CLDN3-positive (T47D, OVCAR-3, Caov-3, MCF-7) cells (Fig. S2).

C-LPNs were prepared using the one-step site-specific conjugation property of h4G3cys in which h4G3cys-conjugated lipid vesicles and PNs fused together after extruding, as shown in Fig. 1A. Plain PNs and the resulting lipid-coated particles exhibited a homogeneous, spherical morphology (Fig. 3A and B). TEM imaging of C-LPNs revealed dark, spherical shapes covered by a thin bright layer. The thin layer was approximately 15 nmol/L thick, indicating successful coverage of PNs by the lipid layer (Fig. 3B). Despite the existence of a thin lipid layer in LPNs, the mean size of LPNs did not significantly differ from that of PNs (Fig. 3C).

Elemental mapping of C-LPNs suggested the presence of carbon and oxygen, the basic backbone elements of PNs. Again, the presence of elemental phosphorus provided reinforcing evidence for lipid coating on the surface of PNs (Fig. 3D). The highest lipid content on particles was obtained at a ratio of 10: 27 (*w/w*). Further increases in the lipid above 10:27 (*w/w*) did not significantly change the lipid content of particles (Fig. 3E). Antibody conjugation efficiency increased with increased feeding concentration of antibody, an effect that saturated
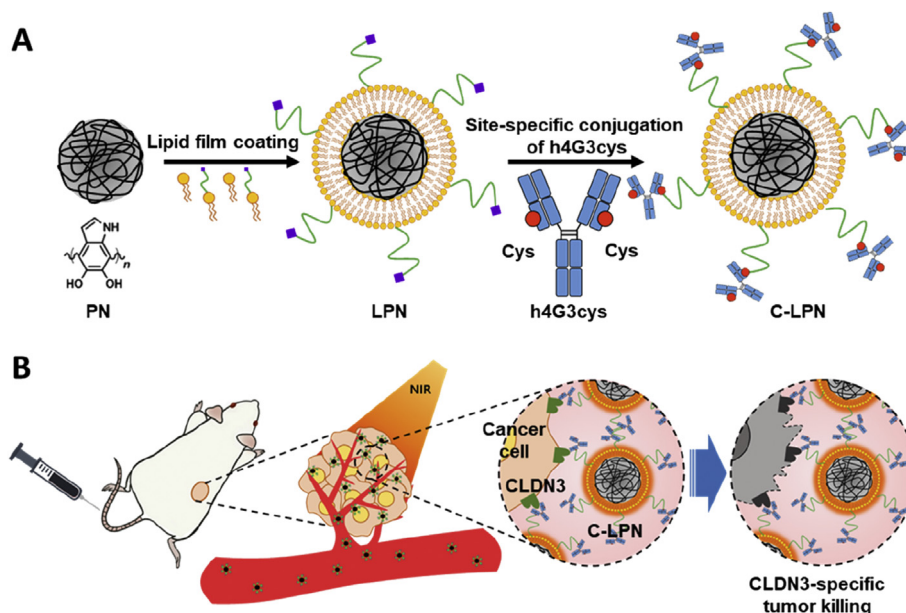
Figure 1   Schematic illustration of C-LPNs preparation and targeted photothermal therapy (PTT) mechanism. (A) PDA core nanoparticles (PNs) were coated with a thin lipid film containing lipid-PEG-maleimide and then conjugated with the cysteine-engineered anti-CLDN3 antibody. Site-specific conjugation at the cysteine group resulted in immobilization of the antibody on the PNs surface in an orientation that maintains antigen-recognition ability. (B) CLDN3-positive tumor cells were targeted by intravenously injected C-LPNs and were ablated by high temperatures induced by NIR irradiation of C-LPNs.
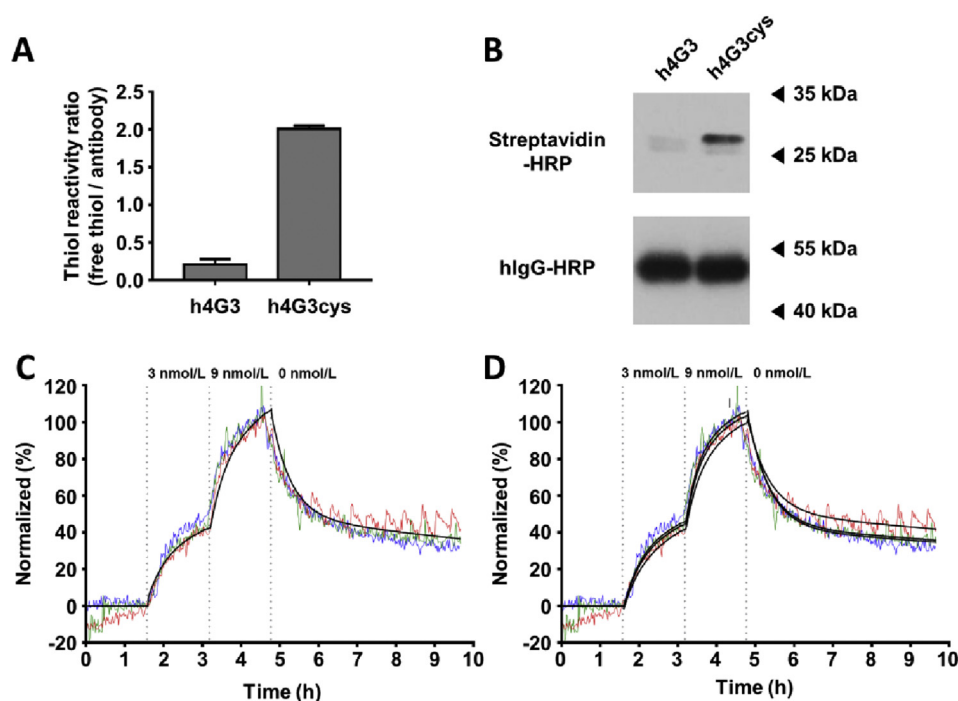
Figure 2 Thiol reactivity and site-specific conjugation of h4G3cys. (A) Thiol reactivities of h4G3 and h4G3cys were evaluated using 4-PDS, and expressed as molar ratios of free thiol groups per antibody. Data represent mean $\pm$ SD ($n = 3$). (B) h4G3 and h4G3cys were conjugated using maleimide-PEG$_2$-biotin, and biotin was detected by Western blotting using SHRP. Human IgG-HRP was used as a loading control. Binding traces of FITC-labeled h4G3cys against CLDN3 on the cell membrane. (C) and(D) TOV-112D or CLDN3/TOV-112D cells were sequentially treated with FITC-labeled h4G3cys at 3 and 9 nmol/L. The cells were then replaced with fresh medium in the dissociation phase. The fluorescence signal was calculated by subtracting the value of the reference cells from that of target cells, and normalized ($n = 3$). The obtained binding curves were fitted by 'one-to-one two-state' model (C) and 'one-to-two' model (D). Three independent experiments curves are shown in red, green, and blue. The fitting curves are shown in black.

when the antibody/PN reaction ratio reached 0.5:1 (*w/w*, Fig. 3F). At 400 μg/mL of sample concentration, the maximum steady-state temperature and surround temperature of C-LPNs was 48.2 and 28.0 °C, respectively (Fig. 3G). Calculated *hs* was given as 20.3 mW/°C based on the time constant obtained from Fig. 3H. The calculated photothermal conversion efficiency (η) of PNs, LPNs, and C-LPNs was 44.1%, 41.7%, and 40.1%, respectively. No significant difference was observed in appearance of PNs, LPNs, and C-LPNs (Fig. 3I).

3.2. Cellular uptake of C-LPNs in CLDN3-positive cells

Cellular binding of C-LPNs to CLDN3-positive cells was monitored by flow cytometry and immunofluorescence. Flow cytometry analysis showed the different expression levels of CLDN3 between Hs578 T cells (Fig. 4A) and T47D cells (Fig. 4B). As compared to Hs578T cells, T47D cells revealed 32-folds higher expression of CLDN3 (Fig. 4C). To visualize whether C-LPNs could target CLDN3-positive cells *via* specific binding of tethered h4G3cys, FITC-labeled lipid was incorporated in the lipid layer of LPNs. Cell surface was stained with an Alexa 555-labeled anti-human IgG antibody. In Hs578T cells lacking CLDN3, FITC and Alexa 555 signals of untreated cells were similar to those of cells treated with IG-LPNs or C-LPNs (Fig. 4D). In contrast, FITC and Alexa 647 signals of T47D cells were higher in the group treated with C-LPNs (Fig. 4E). The FITC (Fig. 4F) or Alexa 647 (Fig. 4G) signals of cells treated with C-LPNs were 33.7- or 53.3-fold higher than those of cells treated with IG-LPNs, respectively. Antibody binding to cell

surfaces was further tested by immunostaining with an Alexa 555-labeled anti-human IgG antibody. Fluorescence images of Hs578T cells were similar following treatment with IG-LPNs or C-LPNs (Fig. 4D). In contrast, T47D cells showed differences in fluorescence between the two groups. Binding of Alexa 555-labeled anti-human IgG antibody was intense only in T47D cells treated with C-LPNs, and not those treated with IG-LPNs (Fig. 4E). TEM showed that attachment of C-LPNs onto CLDN3-negative Hs578T cells was negligible, revealing few nanoparticles per image (Fig. 4G). In contrast, dozens of C-LPNs were observed on CLDN3-positive T47D cells (Fig. 4H).

Moreover, the pellet color of cells treated with nanoparticles was different depending on cell type and nanoparticle type. For CLDN3-negative Hs578T cells, there was no clear difference in the color of cell pellets between IG-LPNs and C-LPNs treatments (Fig. 4I). However, for CLDN3-positive T47D cells, the pellets of cells treated with C-LPNs were much darker than those treated with IG-LPNs (Fig. 4J).

C-LPNs did not exert significant cytotoxicity against Hs578T and T47D cells (Supporting Information Fig. S3). The viability of Hs578T or T47D cells was maintained over 92% in the range of C-LPNs concentrations. In this study, we treated cells with 300 μg/mL of C-LPNs before NIR irradiation. However, even at the concentration of 1000 μg/mL, the treatment with C-LPNs alone did not significantly affect the cell viability. Moreover, there were no significant viability differences between Hs578T and T47D cells.
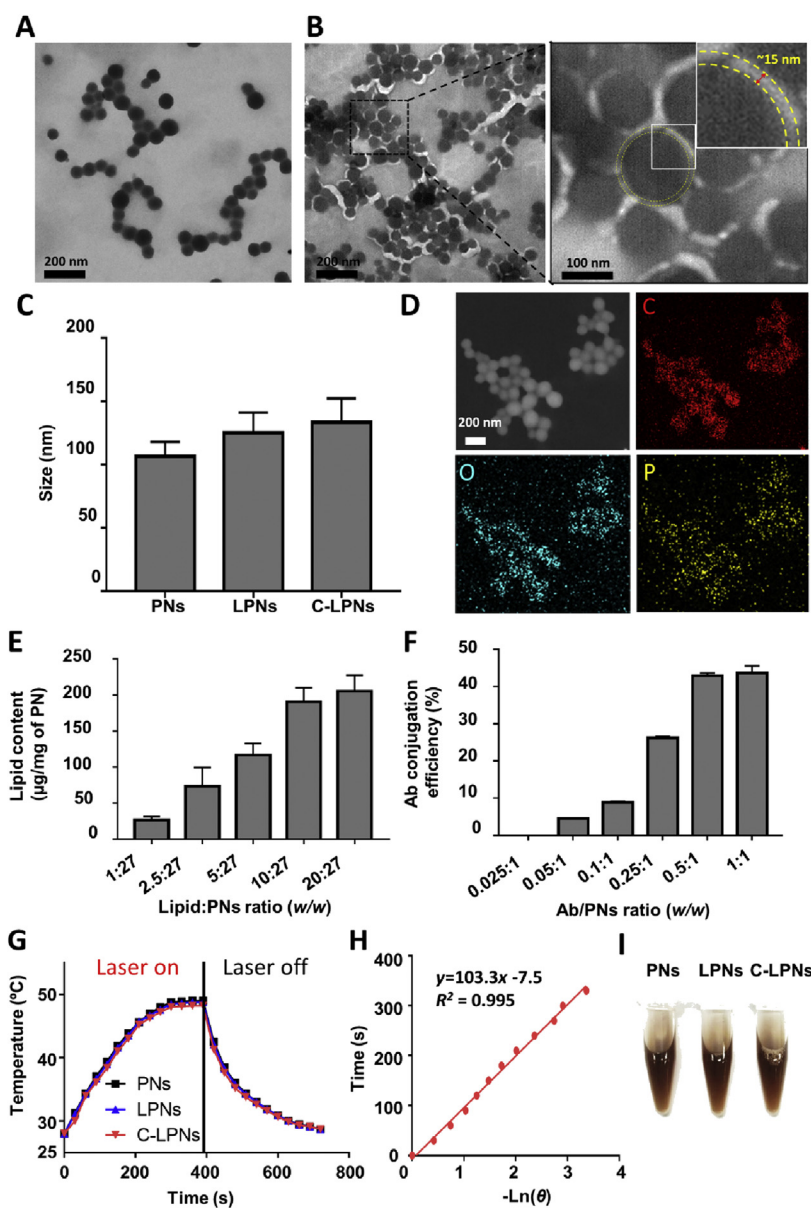
Figure 3 Characterization of nanoparticles. Samples were negatively stained and observed by TEM. TEM images of PNs (A) and C-LPNs (B) reveal a light circle around the PNs particle surface, indicating the presence of a lipid membrane (yellow dashed line). Right Panel: magnified image of black-dashed square in B, which is further magnified in the inset. (C) Average sizes of PNs, LPNs and C-LPNs were measured by dynamic light scattering. Data represents mean $\pm$ SD ($n = 3$). (D) EDS-TEM images of C-LPNs mapping elemental carbon (C), oxygen (O), and phosphorus (P). (E) Quantification of lipid content in each C-LPNs formulated at different lipid:PNs ratios. Data represents mean $\pm$ SD ($n = 3$) (F) Antibody conjugation efficiency was quantified at different feeding antibody:PNs ratios. Data represents mean $\pm$ SD ($n = 3$) (G) Temperatures of samples were recorded during NIR laser irradiation and post irradiation. (H) Time was plotted with '$-\mathrm{Ln}\theta$' obtained from cooling interval of C-LPNs. (I) Photographs of nanoparticles dispersed in culture media.

3.3. In vitro photothermal activity of C-LPNs in CLDN3-positive and -negative cells

The photothermal activity of C-LPNs depended on the expression levels of CLDN3 on tumor cells. Consistent with cell binding results, the increase in temperature of Hs578T cells upon NIR irradiation did not differ between groups treated with IG-LPNs or C-LPNs (Fig. 5A). However, in T47D cells, there was a notable increase in the NIR-responsive temperature increase in the group treated with C-LPNs, but not that treated with IG-LPNs (Fig. 5B).

Quantification of temperature data showed that the temperature upon NIR irradiation reached less than 40 °C in Hs578T cells treated with C-LPNs (Fig. 5C). In contrast, the temperature of C-LPNs-treated T47D cells upon NIR irradiation increased to more than 60 °C—a temperature 26.5 °C higher than that in cells treated with IG-LPNs (Fig. 5D).

The photothermal activity of C-LPNs was correlated with the anticancer efficacy against T47D cells. In the absence of NIR irradiation, neither cell line exhibited significant cell death in either treatment group. Regardless of NIR irradiation and types of
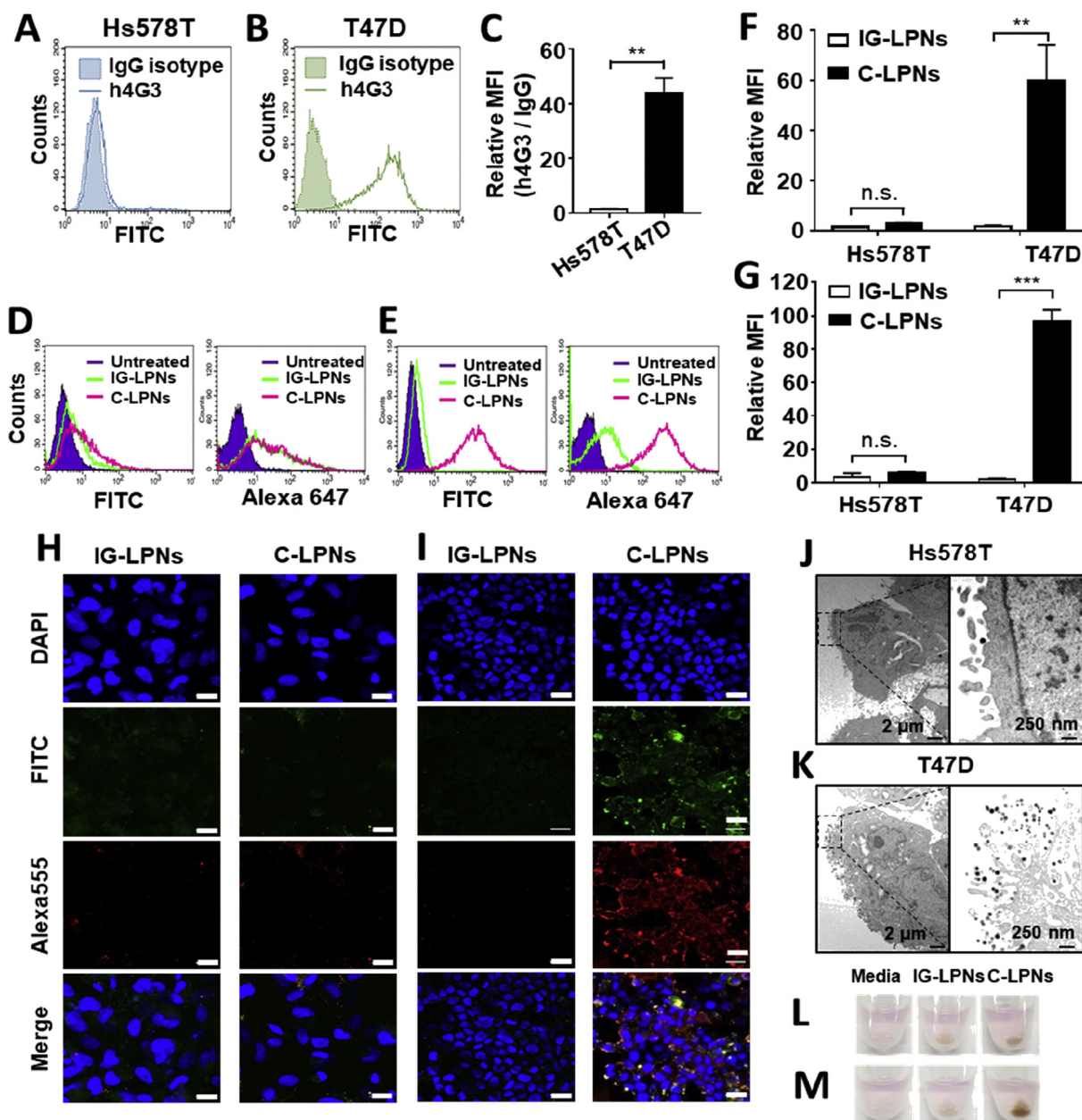
Figure 4 *In vitro* cell-specific binding efficacy of C-LPNs. Expression of CLDN3 in Hs578T (A) and T47D cells (B) was evaluated by flow cytometry. (C) The relative expression of h4G3 over IgG was provided. Data represent mean ± SD ($n = 3$, **$P < 0.01$). Hs578T (D) and T47D cells (E) were treated with FITC-labeled IG-LPNs or C-LPNs for 1 h at 37 °C and harvested. LPNs-conjugated antibodies were detected with an Alexa 647-conjugated anti-hIgG secondary antibody and analyzed by flow cytometry. FITC-positive (F) or Alexa 647 (G)-positive population was analyzed. Data represent mean ± SD ($n = 3$, n.s.: not significant, **$P < 0.01$, ***$P < 0.001$). Hs578T (H) and T47D (I) cells were incubated with FITC-labeled IG-LPN or C-LPN for 1 h at 37 °C, fixed, and then stained with Alexa 555-conjugated anti-human IgG secondary antibody. Cellular fluorescence was observed by confocal microscopy. Blue, green, and red signals represent nuclei, nanoparticles, and conjugated antibodies, respectively. Scale bar = 20 μm. Hs578T (J) and T47D (K) cells were treated with C-LPN for 1 h at 37 °C, and bound C-LPN were observed by TEM. Dark spots are C-LPN. Hs578T (L) and T47D (M) cells were treated with IG-LPN or C-LPN for 1 h and then harvested. Cells were collected by centrifugation and the color of cell pellets was visually inspected.

treatments, Hs578T cell retained the viability higher than 80% (Fig. 6A). In contrast, the viability of T47D cells was significantly reduced to lower than 2% after treatment with C-LPNs followed by NIR irradiation (Fig. 6B). In CLDN3-negative Hs578T cells, fluorescent cell staining data show that the viability of all groups was not affected by the type of nanoparticles, and NIR irradiation (Fig. 6C). However, consistent with WST data, CLDN3-positive T47D cells revealed that the viability was reduced only after the treatment with

C-LPNs and NIR irradiation (Fig. 6D). Thus, C-LPNs display photothermal efficacy against CLDN3-positive cancer cells.

3.4. *In vivo photothermal efficacy of C-LPNs in mice bearing CLDN3-positive tumors*

In agreement with our *in vitro* data, the photothermal activity of C-LPNs was enhanced *in vivo* in a T47D tumor-bearing mouse
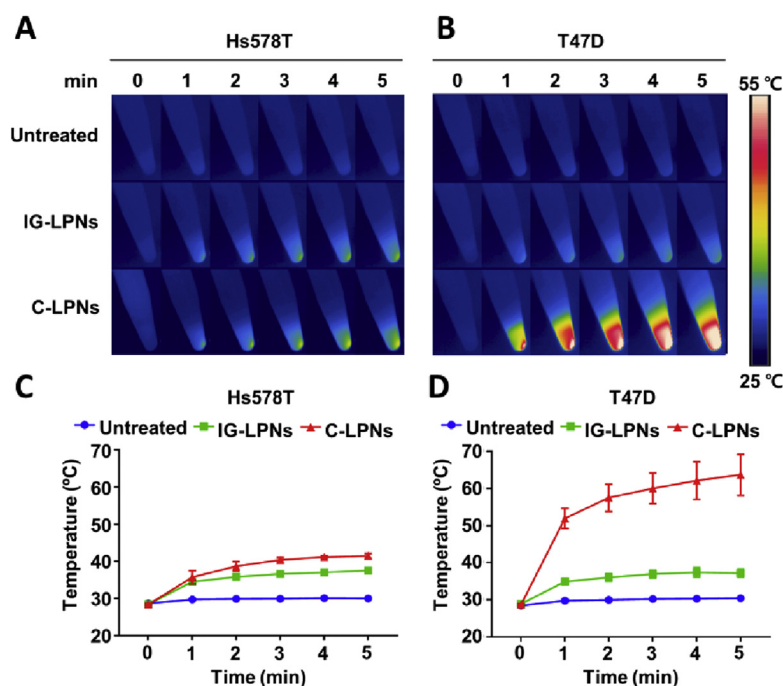
Figure 5 *In vitro* photothermal activity of C-LPNs upon NIR irradiation. Representative thermal images of Hs578T (A) and T47D (B) cell pellets obtained using an infrared thermal camera. Hs578T (C) and T47D (D) cell pellets were irradiated with a NIR laser (808 nm) for 5 min, and temperature changes were monitored every minute using an infrared thermal camera. Data represent mean ± SD ($n = 3$).

model. Tumor accumulation of C-LPNs is demonstrated by *in vivo* imaging of Cy5-labelled nanoparticles (Fig. 7). At one day after injection, C-LPNs showed higher distribution to the tumor tissues than IG-LPNs (Fig. 7A). The *ex vivo* imaging for extracted organs and tissues at 2 days post-dose reveal the higher distribution of C-LPNs to the tumor tissues (Fig. 7B). The fluorescence intensity of tumor tissues was 3.4-fold higher in the group treated with C-LPNs as compared with the group treated with IG-LPNs (Fig. 7C).

Twenty-four hours after intravenous injection of IG-LPNs or C-LPNs, tumors were irradiated with NIR. Thermal images also displayed heat spread throughout the tumor area in C-LPNs-treated mice, whereas thermal images of untreated and IG-LPNs-treated mice showed that heat was localized at the point of irradiation (Fig. 8B). Upon NIR irradiation, the temperature of tumor sites reached as high as 60 °C in mice treated with C-LPNs, a temperature 10.9 and 14.8 °C higher than that mice treated with IG-LPNs or left untreated, respectively (Fig. 8C).

T47D tumors continued to grow after NIR irradiation in groups treated with IG-LPNs (Fig. 8D). Moreover, T48D tumor growth was observed in the group treated with C-LPNs without NIR irradiation. However, upon NIR irradiation, tumors treated with C-LPNs did not show increased growth and were completely ablated at day 30 after a single exposure to NIR (Fig. 8D). Representative photographs of mice in different treatment groups showed that tumor sites turned black, forming a scab at Day 8. At Day 20, the black scab had detached from the irradiated site, revealing a clean, tumor-ablated site (Fig. 8E). Body weight data show that the NIR irradiation and administration of various LPNs did not reduce body weights of mice (Fig. 8F), indicating that LPNs treatments are relatively non-toxic.

H&E staining revealed the different histology of the group treated with C-LPNs plus NIR (Fig. 9A). Compared with other groups, the group treated with C-LPNs plus NIR showed darker and fragmented nuclear staining. TUNEL assay showed the highest

population of apoptotic cells in the group treated with C-LPNs plus NIR (Fig. 9B). In other groups, there was little sign of apoptosis.

4. Discussion

In this study, site-specific conjugation of an anti-CLDN3 antibody to the surfaces of LPNs was demonstrated to provide greater nanoparticle uptake into CLDN3-positive tumor cells and *in vivo* tumor ablation upon NIR irradiation. LPNs were used for conferring NIR photoresponsiveness and cysteine-directed maleimide conjugation of antibody.

As a photoresponsive core material, we chose PDA-synthesized by a facile pH-dependent polymerization process from dopamine[6], owing to its simplicity, biodegradability, and biocompatibility. PDA has been exploited in recent studies as stable material for biocapacitor[20] or drug carriers for cancer photothermal therapy[21,22]. PNs formed from PDA are expected to degrade to dopamine monomers, quinine, and PNs segments[23,24]. The degradation of melanin with a PNs-like structure has been shown to take more than 8 weeks *in vivo*[23]. It has been reported that PDA is degraded in the cytoplasm *via* the reducing catalytic activity of glutathione[25]. It has been shown that intravenous injection of PNs does not cause histological or hematological toxicity in mice[6].

Despite the merits of PNs, their catechol-rich surfaces are not suitable for specific conjugation with cysteine groups of anti-CLDN3 antibodies containing a genetically introduced cysteine group. In this study, we coated the surfaces of polydopamine nanoparticles with maleimide-functionalized polyethyleneglycol lipid derivative. The surface coating with polyethyleneglycol can provide the higher stability in the bloodstream. In addition, the surface coating can prevent the nonspecific conjugation of h4G3cys to the catechol moieties of polydopamine nanoparticles.
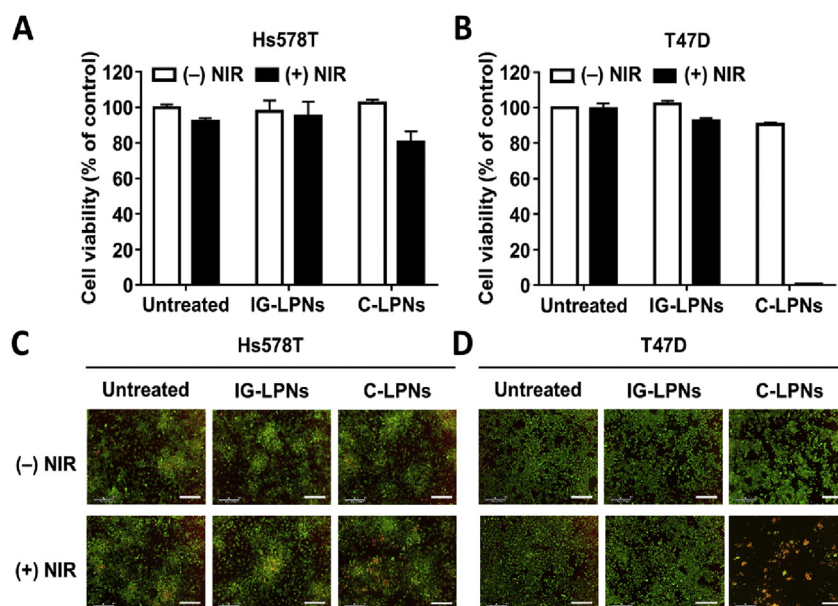
Figure 6 *In vitro* anticancer efficacy of C-LPNs-mediated PTT. Hs578T (A, C) and T47D (B, D) cells were treated with IG-LPNs or C-LPNs for 1 h and harvested by centrifugation. The resulting pellets were irradiated with a NIR laser (808 nm) for 5 min, seeded on a 96-well plate, and incubated for 24 h. (A) and (B) The viability of cells was determined using a WST assay. (C) and (D) Live and dead cells were visualized by staining with calcein-AM and propidium iodide, respectively. Scale bar $= 300$ μm. Data represent mean $\pm$ SD ($n = 3$).

The surface coating with a maleimide-functionalized polyethyleneglycol can hinder the access of amine or thiol groups of h4G3cys to the catechol moieties of polydopamine. Moreover, the external maleimide end of pegylated lipid enables the preferential binding with thiol group at the genetically introduced cysteine residue of h4G3cys. Thus, the surfaces of PNs were modified with lipids containing maleimide functional groups. A number of catechol, amine, and carboxylic groups, as well as the hydrophobic backbone of a polyaromatic ring, are exposed on the surface of PNs[26]. Lipid molecules hydrophobically adhere to the surfaces of PNs. Conjugation of specific cysteine groups in h4G3cys to maleimide may result in a covalent carbon−sulfur bond. A maleimide linker has been used for the approved antibody-drug conjugate, Adcetris[27].

As lipid components of LPNs, we tested lipid maleimide derivatives as well as DPPC, DPPG, and DSPE-PEG$_{2000}$. DPPC, DPPG, and DSPE-PEG$_{2000}$ have been used as components of clinically approved liposome products[28−30]. DPPG is a negatively charged lipid that stabilizes the dispersion of LPNs in aqueous solutions. PEGylated lipid was used to provide hydrophilic "clouds" on LPNs surfaces, which can reduce the adhesion of nonspecific opsonins in the blood circulation *in vivo*[31,32].

One advantage of cysteine-specific conjugation of antibodies in C-LPNs is its ability to control orientation of the antibody. The conjugation of antibody to the surface of nanoparticles is typically accomplished through free amine or carboxyl groups on antibodies using cross-linking agents. However, this approach generates heterogeneous immunoconjugates and cannot guarantee the optimal orientation and functionality of the conjugated antibody owing to non-specific coupling. For site-specific conjugation, we used an antibody in which a cysteine residue was genetically introduced by replacing Q124 in the light chain of h4G3. The free thiol reactivity of the cysteine residue in the h4G3 antibody allows direct site-specific conjugation[16]. Indeed, we observed that the molecularly engineered cysteine-containing

anti-CLDN3 antibody was conjugated to LPNs to a greater extent than a non-engineered anti-CLDN3 antibody. This observation supports the conclusion that cysteine-specific conjugation of h4G3cys antibody on LPNs creates optimal orientation and functionality.

Although h4G3cys has cysteine at each light chain, our data support that there was low chance of conjugation with other nanoparticles. Fig. 3C shows that the mean sizes of LPNs and C-LPNs did not significantly differ. Moreover, we found that there is no sign of aggregate formation in the size distribution of C-LPNs (Supporting Information Fig. S4). The low reactivity of unconjugated cysteine with maleimide groups on other particles would be explained in part by the hydrophilic clouding effect of PEG shell. Once conjugated, the other cysteine residue will be buried inside the hydrophilic shell, with limited chances to interacting with maleimide groups of other particles. In addition, our antibody conjugation condition was established to saturate the maleimide groups on nanoparticles. Fig. 3F shows that the conjugation efficiency reached to the saturation level at the ratio of antibody to PNs (0.5:1). The consumption of available maleimide groups on nanoparticles may have contributed to minimize the interaction with the unreacted cysteine residue of other nanoparticles.

The genetic engineering of cysteine introduction to h4G3 did not affect the binding to CLDN3 receptors. To introduce cysteine residues for direct conjugation, we chose the mutation Q124C in the light chain. Q124C is positioned in light chain constant region, and known to be not involved in antigen binging capacity. To confirm whether the genetic introduction of cysteine residue did not alter the binding affinity to the target receptor, we compared the binding of h4G3 and h4G3cys to cell lines with different extents of CLDN3 receptor expression levels. Regardless of CLDN3 receptor expressions, similar binding patterns were observed for h4G3 and h4G3cys in CLDN3-negative cells (TOV-112D, Hs578T), CLDN3-expressing stable cells (CLDN3/TOV-112D), and CLDN3-positive (T47D, OVCAR-3, Caov-3 and MCF-7)
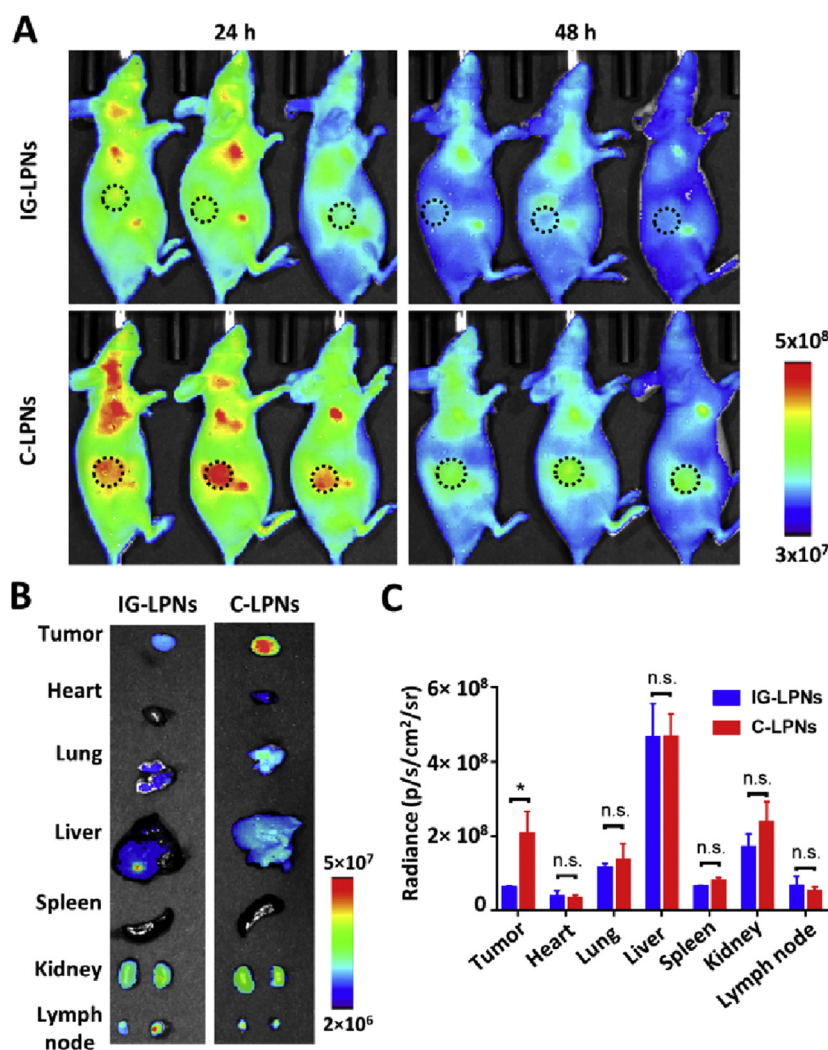
Figure 7 *In vivo* distribution in a mouse xenograft model. Mice bearing T47D tumors were intravenously injected with Cy5-labelled IG-LPNs or Cy5-labelled C-LPNs. (A) Molecular imaging of mice was done at various time point post-dose. The dotted circle marks the tumor site. (B) *Ex vivo* imaging of organs and tumor tissues at 48 h post-dose. (C) The mean image intensity of each organ was quantified. ($n = 3$, n.s.: not significant, $*P < 0.05$).

cells (Fig. S2). Notably, in CLDN3-positive cells, both h4G3 and h4G3cys similarly showed higher binding to the cells compared to control IgG antibody.

In this study, for comparison with C-LPNs, we used IG-LPNs made with genetically cysteine-introduced IgG, rather than wild type h4G3-conjugated nanoparticles (C-WT-LPN). Indeed, we compared the cell binding of C-LPNs with that of C-WT-LPNs. The CLDN3-positive cell binding of C-WT-LPNs was negligible to that of C-LPNs (Supporting Information Fig. S5). The difference could be due to the lower antibody amounts on the nanoparticle surface rather than to the higher targeting ability of C-LDNs. To test the targeting ability of h4G3cys, we genetically engineered the IgG isotype Q124C to express cysteine residue. The genetic introduction of cysteine group in Q124C may allow similar binding of antibodies to LPNs *via* maleimide and thiol chemistry, and enable to test only the targeting function of h4G3cys.

The integrity of the Fab conformation could result in efficient binding to CLDN3 on tumor cell surfaces. A recent report describing tethering of an antibody to Fc-binding peptides on the surfaces of liposomes highlights the importance of antibody orientation[33]. In this latter study, the controlled orientation of antibody binding was shown to provide higher binding to target cell surfaces compared to nanoparticles with a nonspecifically conjugated antibody.

C-LPNs were effectively taken up by CLDN3-positive tumor cells, but not by CLDN3-negative tumor cells. There was some non-specific binding to Hs578T cells, as evidenced by the similar cellular uptake of C-LPNs and IG-LPNs. This phenomenon would be in part attributed to nonspecific biding and endocytosis of anionic liposome by cancer cells *via* micropinocytosis[34]. However, non-specific binding to the cell membrane did not result in significant *in vitro* photothermal activity in the CLDN3-negative cell line, whereas C-LPNs induced high temperature and cell death after NIR irradiation in the CLDN3-positive cell line. Since the efficacy of C-LPNs is exerted by local NIR irradiation of the tumor site, side effects of modest non-specific binding to normal cells or tissues would be limited.

We observed the dark brown color of the cells treated with C-LPNs (Fig. 4M). The brown color is due to the dark brown color
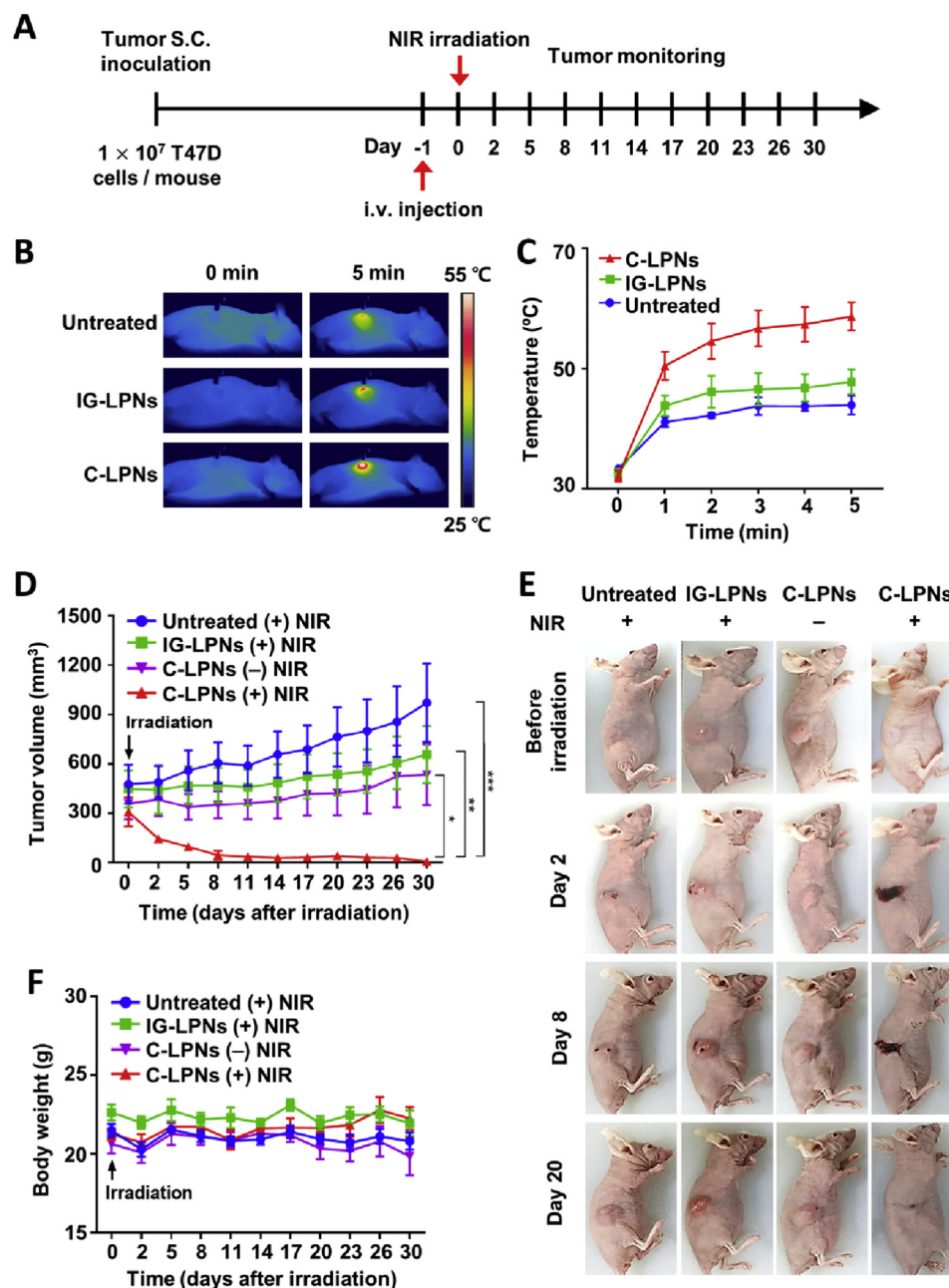
Figure 8 *In vivo* photothermal efficacy in a mouse xenograft model. Mice bearing T47D tumors were intravenously injected with IG-LPNs or C-LPNs. (A) Schematic illustration of the tumor inoculation and treatment schedule. After 24 h, the tumor was irradiated with an NIR laser (808 nm) for 5 min, and the temperature was visualized (B) and quantified (C) every minute using an infrared thermal camera. (D) After NIR irradiation, tumor sizes were monitored twice a week, as described in Methods section. (E) Representative photographs of mice bearing T47D tumors before and after irradiation on Days 2, 8, and 20. (F) Body weights of mice were monitored twice a week after single NIR irradiation. Data represent means $\pm$ SEM ($n = 4$; $^*P < 0.05$, $^{**}P < 0.01$, $^{***}P < 0.001$).

of C-LPNs. Fig. 3I shows the dark brown colors for both types of nanoparticles. The different brown colors of cell pellets visualize the extent of brown nanoparticle binding. The darker brown color of the cells treated with C-LPNs supports the higher binding of brown C-LPNs to CLDN3-positive cells.

In mice bearing CLDN3-positive tumors, a single exposure to NIR irradiation completely ablated tumors in mice treated with C-LPNs. Such potent photothermal efficacy is attributable to enhanced uptake of C-LPNs by tumor cells. Mice treated with C-LPNs without NIR irradiation showed continued growth of

tumors, indicating that it is unlikely that anti-CLDN3 antibody conjugation alone exerts a notable anticancer effect, further highlighting the importance of NIR irradiation.

Although in this study we used T47D breast cancer cells as a model of CLDN3-positive tumor cells, C-LPNs could be used for other types of CLDN3-positive tumors. It has been reported that CLDN3 is overexpressed in a variety of cancers, including ovarian, gastric, colorectal, prostate, and pancreatic cancer[14,35−37]. Notably, overexpression of CLDN3 is related to a poor clinical outcome[38−41]. In addition, CLDNs, which are tight junction
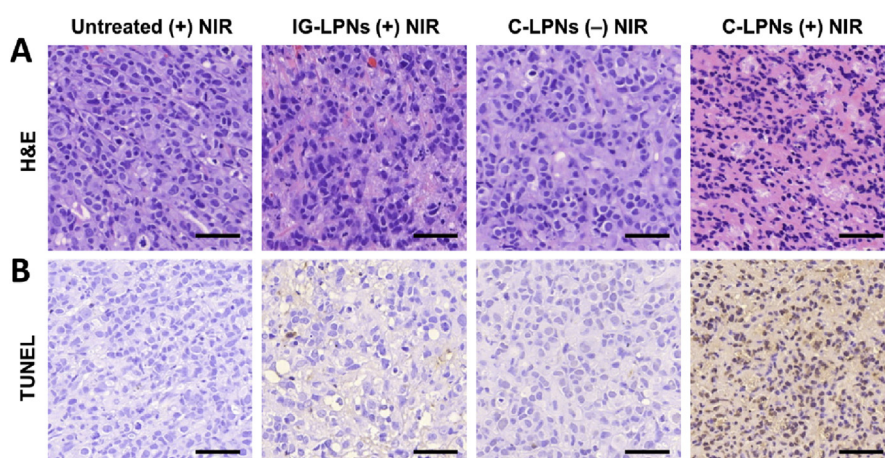
Figure 9 Histology and apoptosis of tumor tissues. T47D tumor-bearing mice were irradiated with a NIR laser (808 nm) at one day post-dose of nanoparticles. One day after NIR irradiation, the tumor tissues were subjected to H&E staining and TUNEL assay. Scale bar = 50 μm.

proteins, are attractive cancer biomarkers owing to their accessibility in cancer cells compared with normal cells. During epithelial tumorigenesis, misorientation of the cell division axis causes out-of-plane division and exposes CLDNs that are normally inaccessible in tight junctions. Hence, the accessability of CLDNs is increased in cancer cells but is limited in normal epithelial cells, allowing CLDNs to act as cancer-specific biomarkers[42]. Previously, our group developed a human monoclonal antibody (h4G3) against CLDN3 and demonstrated the possibility of using immunoconjugates against CLDN3-overexpressing carcinomas[43]. In the study, we identified that the extracellular loop 2 domain of CLDN3 is involved in the recognition of h4G3[43].

CLDN3 could be a viable target for future clinical translation. Ongoing clinical trials use antibodies specific for various CLDNs, including IMAB027 and IMAB362, which target CLDN6 and CLDN18.2, respectively. A first-in-humans phase I/II dose-escalation study of IMAB027 against recurrent advanced ovarian cancer was recently completed (NCT02054351). In the case of IMAB362, a single dose safety study (phase I), a safety study in combination with zoledronic acid and interleukin-2 (phase I), a repeated monotherapy study (phase IIA), and an efficacy/safety study (phase IIB) in combination with the EOX (epirubicin, oxaliplatin, and capecitabine) regimen for advanced gastric cancer have also been completed[44]. Patients are currently being recruited for a phase III efficacy study of IMAB362 in combination with capecitabine and oxaliplatin (CAPOX), or mFOLFOX6 chemotherapy for gastric and gastroesophageal junction (GEJ) cancer (NCT03653507 and NCT03504397). These cases underscore the clinical applicability of targeting CLDN3 and support the expectation of favorable results.

For clinical translation, NIR phototherapy can be applied to the treatment of localized and light-accessible tumors. One concern is the limited tissue penetration of NIR light. Diverse types of NIR light sources such as fiber optic diffusers have been reported to provide light penetration to deeper tumors. Irradiation of light in NIR-II window has been shown to penetrate deeper tissues[45,46]. C-LPNs could be relevant to the treatment of CLDN3-positive and NIR light-accessible tumors, such as ovarian and prostate tumors. For example, C-LPNs in conjunction with NIR irradiation may help to remove residual ovarian cancer peritoneal metastasis remaining after surgery. In addition, prostate cancer could be treated by C-LPNs injection and NIR irradiation without requiring a biopsy. Previously, PTT using gold nanoparticles revealed favorable outcomes in men with low- or intermediate-risk, localized prostate cancer[47]. PTT has been reported to induce systemic antitumor responses that prevent metastasis or tumor recurrence[6,48]. On the other hand, various studies have reported that PTT can synergize with chemotherapy to provide a more efficacious regime[49]. Therefore, our C-LPNs would be promising agents for clinical approaches as a single therapy or as combined strategies with immunotherapy and chemotherapy.

In conclusion, the site-specific conjugation of h4G3cys to maleimide groups of LPNs in C-LPNs enabled controlled antibody orientation and higher target cell uptake. The complete ablation of tumors in C-LPNs-treated mice by a single exposure to NIR irradiation suggests the potential translation of this platform to laser light-induced PTT of CLDN3-positive cancers.

Acknowledgments

Author contributions

Gayong Shim, Yu-Kyoung Oh and Young Kee Shin designed the research. Hobin Yang and Quoc-Viet Le carried out the experiments and performed data analysis. Hobin Yang and Quoc-Viet Le wrote the manuscript. Gayong Shim, Yu-Kyoung Oh and Young Kee Shin revised the manuscript. All of the authors have read and approved the final manuscript.

Conflicts of interest

The authors have no conflicts of interest to declare.

Appendix A.   Supporting information

Supporting data to this article can be found online at https://doi.org/10.1016/j.apsb.2020.07.006.

References

1. Liang S, Li C, Zhang C, Chen Y, Xu L, Bao C, et al. CD44v6 monoclonal antibody-conjugated gold nanostars for targeted photo-acoustic imaging and plasmonic photothermal therapy of gastric cancer stem-like cells. *Theranostics* 2015;**5**:970–84.
2. Golkar N, Tamaddon AM, Samani SM. Effect of lipid composition on incorporation of trastuzumab-PEG-lipid into nanoliposomes by post-insertion method: physicochemical and cellular characterization. *J Liposome Res* 2016;**26**:113–25.
3. Chen F, Ma K, Madajewski B, Zhuang L, Zhang L, Rickert K, et al. Ultrasmall targeted nanoparticles with engineered antibody fragments for imaging detection of HER2-overexpressing breast cancer. *Nat Commun* 2018;**9**:4141.
4. Yang YS, Moynihan KD, Bekdemir A, Dichwalkar TM, Noh MM, Watson N, et al. Targeting small molecule drugs to T cells with antibody-directed cell-penetrating gold nanoparticles. *Biomater Sci* 2018;**7**:113–24.
5. Li C, Wang J, Wang Y, Gao H, Wei G, Huang Y, et al. Recent progress in drug delivery. *Acta Pharm Sin B* 2019;**9**:1145–62.
6. Le QV, Suh J, Choi JJ, Park GT, Lee JW, Shim G, et al. *In situ* nanoadjuvant-assembled tumor vaccine for preventing long-term recurrence. *ACS Nano* 2019;**13**:7442–62.
7. Hadjipanayis CG, Machaidze R, Kaluzova M, Wang L, Schuette AJ, Chen H, et al. EGFRvIII antibody-conjugated iron oxide nano-particles for magnetic resonance imaging-guided convection-enhanced delivery and targeted therapy of glioblastoma. *Cancer Res* 2010;**70**:6303–12.
8. Liu Y, Li K, Liu B, Feng SS. A strategy for precision engineering of nanoparticles of biodegradable copolymers for quantitative control of targeted drug delivery. *Biomaterials* 2010;**31**:9145–55.
9. Mu X, Zhang F, Kong C, Zhang H, Zhang W, Ge R, et al. EGFR-targeted delivery of DOX-loaded Fe$_3$O$_4$@polydopamine multifunctional nanocomposites for MRI and antitumor chemo-photothermal therapy. *Int J Nanomed* 2017;**12**:2899–911.
10. Dennler P, Fischer E, Schibli R. Antibody conjugates: from heterogeneous populations to defined reagents. *Antibodies* 2015;**4**:197–224.
11. Colombo M, Sommaruga S, Mazzucchelli S, Polito L, Verderio P, Galeffi P, et al. Site-specific conjugation of ScFvs antibodies to nanoparticles by bioorthogonal strain-promoted alkyne-nitrone cycloaddition. *Angew Chem Int Ed* 2012;**51**:496–9.
12. Mustafaoglu N, Kiziltepe T, Bilgicer B. Site-specific conjugation of an antibody on a gold nanoparticle surface for one-step diagnosis of prostate specific antigen with dynamic light scattering. *Nanoscale* 2017;**9**:8684–94.
13. Chen S, Florinas S, Teitgen A, Xu ZQ, Gao C, Wu H, et al. Controlled Fab installation onto polymeric micelle nanoparticles for tuned bioactivity. *Sci Technol Adv Mater* 2017;**18**:666–80.
14. Ding L, Lu Z, Lu Q, Chen YH. The claudin family of proteins in human malignancy: a clinical perspective. *Cancer Manag Res* 2013;**5**:367–75.
15. Kwon MJ. Emerging roles of claudins in human cancer. *Int J Mol Sci* 2013;**14**:18148–80.
16. Shinmol/Li D, Taguchi E, Iwano J, Yamaguchi T, Masuda K, Enokizono J, et al. One-step conjugation method for site-specific antibody–drug conjugates through reactive cysteine-engineered antibodies. *Bioconjugate Chem* 2016;**27**:1324–31.
17. Jose C, Amra K, Bhavsar C, Momin M, Omri A. Polymeric lipid hybrid nanoparticles: properties and therapeutic applications. *Crit Rev Ther Drug* 2018;**35**:555–88.
18. Hein R, Uzundal CB, Hennig A. Simple and rapid quantification of phospholipids for supramolecular membrane transport assays. *Org Biomol Chem* 2016;**14**:2182–5.
19. Liu X, Li B, Fu F, Xu K, Zou R, Wang Q, et al. Facile synthesis of biocompatible cysteine-coated CuS nanoparticles with high photo-thermal conversion efficiency for cancer therapy. *Dalton Trans* 2014;**43**(30):11709–15.
20. Yang L, Gu B, Chen Z, Yue Y, Wang W, Zhang H, Liu X. Synthetic biopigment supercapacitors. *ACS Appl Mater Interfaces* 2019;**11**:42671–9.
21. Zhou Z, Yan Y, Wang L, Zhang Q, Cheng Y. Melanin-like nanoparticles decorated with an autophagy-inducing peptide for efficient targeted photothermal therapy. *Biomaterials* 2019;**203**:63–72.
22. Tian Y, Wang X, Zhao S, Liao X, Rizwan M, Wang Y, Zhang C, Lu G. JQ1-loaded polydopamine nanoplatform inhibits c-myc/programmed cell death ligand 1 to enhance photothermal therapy for triple-negative breast cancer. *ACS Appl Mater Interfaces* 2019;**11**:46626–36.
23. Bettinger CJ, Bruggeman JP, Misra A, Borenstein JT, Langer R. Biocompatibility of biodegradable semiconducting melanin films for nerve tissue engineering. *Biomaterials* 2009;**30**:3050–7.
24. Jin L, Yuan F, Chen C, Wu J, Gong R, Yuan G, et al. Degradation products of polydopamine restrained inflammatory response of LPS-stimulated macrophages through mediation TLR-4-MYD88 dependent signaling pathways by antioxidant. *Inflammation* 2019;**42**:658–71.
25. Hao YN, Zheng AQ, Guo TT, Shu Y, Wang JH, Johnson O, et al. Glutathione triggered degradation of polydopamine to facilitate controlled drug release for synergic combinational cancer treatment. *J Mater Chem B* 2019;**7**:6742–50.
26. Liebscher J, Mrowczynski R, Scheidt HA, Filip C, Hadade ND, Turcu R, et al. Structure of polydopamine: a never-ending story?. *Langmuir* 2013;**29**:10539–48.
27. Richardson NC, Kasamon YL, Chen H, de Claro RA, Ye J, Blumenthal GM, et al. FDA approval summary: brentuximab vedotin in first-line treatment of peripheral T-cell lymphoma. *Oncologist* 2019;**24**:e180–7.
28. Bulbake U, Doppalapudi S, Kommineni N, Khan W. Liposomal formulations in clinical use: an updated review. *Pharmaceutics* 2017;**9**:12.
29. Wang N, Chen M, Wang T. Liposomes used as a vaccine adjuvant-delivery system: from basics to clinical immunization. *J Control Release* 2019;**303**:130–50.
30. Crommelin DJA, van Hoogevest P, Storm G. The role of liposomes in clinical nanomedicine development. What now? Now what?. *J Control Release* 2020;**318**:256–63.
31. Suk JS, Xu Q, Kim N, Hanes J, Ensign LM. PEGylation as a strategy for improving nanoparticle-based drug and gene delivery. *Adv Drug Deliv Rev* 2016;**99**:28–51.
32. Zahednezhad F, Saadat M, Valizadeh H, Zakeri-Milani P, Baradaran B. Liposome and immune system interplay: challenges and potentials. *J Control Release* 2019;**305**:194–209.
33. Shim G, Kim D, Lee S, Chang RS, Byun J, Oh YK. Staphylococcus aureus-mimetic control of antibody orientation on nanoparticles. *Nanomedicine* 2019;**16**:267–77.
34. Kang JH, Jang WY, Ko YT. The effect of surface charges on the cellular uptake of liposomes investigated by live cell imaging. *Pharm Res* 2017;**34**:704–17.
35. Ouban A, Ahmed AA. Claudins in human cancer: a review. *Histol Histopathol* 2010;**25**:83–90.
36. Singh AB, Sharma A, Dhawan P. Claudin family of proteins and cancer: an overview. *J Oncol* 2010;**2010**:541957.
37. English DP, Santin AD. Claudins overexpression in ovarian cancer: potential targets for *Clostridium perfringens enterotoxin* (CPE) based diagnosis and therapy. *Int J Mol Sci* 2013;**14**:10412–37.
38. Martin TA, Mason MD, Jiang WG. Tight junctions in cancer metastasis. *Front Biosci* 2011;**16**:898–936.
39. Tabaries S, Siegel PM. The role of claudins in cancer metastasis. *Oncogene* 2017;**36**:1176–90.
40. Zhang L, Wang Y, Zhang B, Zhang H, Zhou M, Wei M, et al. Claudin-3 expression increases the malignant potential of lung adenocarcinoma cells: role of epidermal growth factor receptor activation. *Oncotarget* 2017;**8**:23033–47.
41. Jääskelainen A, Soini Y, Jukkola-Vuorinen A, Auvinen P, Haapasaari KM, Karihtala P. High-level cytoplasmic claudin 3

expression is an independent predictor of poor survival in triple-negative breast cancer. *BMC Cancer* 2018;**18**:223.

42. Saeki R, Kondoh M, Uchida H, Yagi K. Potency of claudin-targeting as antitumor therapy. *Mol Cell Pharmacol* 2010;**2**:47−51.

43. Yang H, Park H, Lee YJ, Choi JY, Kim T, Rajasekaran N, et al. Development of human monoclonal antibody for claudin-3 over-expressing carcinoma targeting. *Biomolecules* 2019;**10**:51.

44. Singh P, Toom S, Huang Y. Anti-claudin 18.2 antibody as new targeted therapy for advanced gastric cancer. *J Hematol Oncol* 2017;**10**:105.

45. Okuyama S, Nagaya T, Sato K, Ogata F, Maruoka Y, Choyke PL, et al. Interstitial near-infrared photoimmunotherapy: effective treatment areas and light doses needed for use with fiber optic diffusers. *Oncotarget* 2018;**9**:11159−69.

46. Ge X, Fu Q, Bai L, Chen B, Wang R, Gao S, et al. Photoacoustic imaging and photothermal therapy in the second near-infrared window. *New J Chem* 2019;**43**:8835−51.

47. Rastinehad AR, Anastos H, Wajswol E, Winoker JS, Sfakianos JP, Doppalapudi SK, et al. Gold nanoshell-localized photothermal ablation of prostate tumors in a clinical pilot device study. *Proc Natl Acad Sci U S A* 2019;**116**:18590−6.

48. Le QV, Choi J, Oh YK. Nano delivery systems and cancer immuno-therapy. *J Pharm Investig* 2018;**48**:527−39.

49. Phung DC, Nguyen HT, Phuong Tran TT, Jin SG, Yong CS, Truong DH, et al. Combined hyperthermia and chemotherapy as a synergistic anticancer treatment. *J Pharm Investig* 2019;**49**:519−26.